

# PCCP

Accepted Manuscript



This is an *Accepted Manuscript*, which has been through the Royal Society of Chemistry peer review process and has been accepted for publication.

*Accepted Manuscripts* are published online shortly after acceptance, before technical editing, formatting and proof reading. Using this free service, authors can make their results available to the community, in citable form, before we publish the edited article. We will replace this *Accepted Manuscript* with the edited and formatted *Advance Article* as soon as it is available.

You can find more information about *Accepted Manuscripts* in the [Information for Authors](#).

Please note that technical editing may introduce minor changes to the text and/or graphics, which may alter content. The journal's standard [Terms & Conditions](#) and the [Ethical guidelines](#) still apply. In no event shall the Royal Society of Chemistry be held responsible for any errors or omissions in this *Accepted Manuscript* or any consequences arising from the use of any information it contains.

# S...O Chalcogen Bonding in Sulfa Drugs: Insights from Multipole Charge Density and X-ray Wavefunction of Acetazolamide

Cite this: DOI: 10.1039/x0xx00000x

Received 00th January 2012,  
Accepted 00th January 2012

DOI: 10.1039/x0xx00000x

www.rsc.org/

*Dedicated to Mr. K. R. Sivanandan on the occasion of his retirement\**

Sajesh P. Thomas,<sup>a,b</sup> Dylan Jayatilaka<sup>a</sup> and T. N. Guru Row<sup>\*b</sup>

Experimental charge density analysis combined with the quantum crystallographic technique of X-ray wavefunction refinement (XWR) provides quantitative insights into the intra and intermolecular interactions formed by acetazolamide, a diuretic drug. Firstly, the analysis of charge density topology at intermolecular level shows the presence of exceptionally strong interaction motifs such as a DDAA-AADD (D-donor, A-acceptor) type quadruple hydrogen bond motif and a sulfonamide dimer synthon. The nature and strength of intra-molecular S...O chalcogen bonding has been characterized using descriptors from multipole model (MM) and XWR. Although pure geometrical criteria suggest the possibility of two intra-molecular S...O chalcogen bonded ring motifs, only one of them satisfies the “orbital geometry” so as to exhibit an interaction in terms of electron density bond path and bond critical point. The presence of ‘ $\sigma$ -hole’ on sulfur atom leading to the S...O chalcogen bond has been visualized on electrostatic potential surface and Laplacian isosurfaces close to the ‘reactive surface’. Electron localizability indicator (ELI) and Roby bond orders derived from the ‘experimental wave function’ provide insights into the nature of S...O chalcogen bonding.

## Introduction

Non-covalent intra-molecular interactions that are capable of controlling conformations have significance in various fields of structural chemistry. Being able to predict molecular conformations can be crucial in elucidating drug-protein interaction motifs (docking studies), building initial geometry for computational crystal structure prediction, solving crystal structures from powder XRD patterns (*ab initio* structure determination) etc. While the conformation-locking potential of classical hydrogen bonds are known, that of the weak interactions such as C–H...O and C–H...N hydrogen bonds have also been reported recently.<sup>1</sup> Besides, novel non-bonding interaction types such as halogen bonding,<sup>2,3</sup> chalcogen bonding,<sup>4,6</sup> pnicoen bonding,<sup>7</sup> carbon bonding<sup>8,9</sup> etc are also being explored by structural chemists in various inter and intra-molecular contexts. Among these interactions, halogen bonding and chalcogen bonding are known to play key roles in biological activity<sup>10</sup> and in supramolecular recognition.<sup>2,4</sup> Recently, we have evaluated the conformation locking potential of intramolecular S...O chalcogen bonding in sulfamethizole, a sulfonamide antibiotic.<sup>5</sup> Charge density analyses on a structurally similar drug, sulfathiazole that exhibits intramolecular S...O interactions in its polymorphs have also been reported by Farrugia et al.<sup>11</sup> Destro *et al* have reported the electron density features of S...O interaction in an angiotensin II receptor antagonist molecule via experimental charge density

analysis (although for a relatively large S...O interaction distance of 3.199 Å).<sup>12,13</sup> Recently Scheiner et al have analysed the stabilizing effect of S...O chalcogen bond in the molecular geometries of substituted phenyl-SF<sub>3</sub> molecules via density functional methods.<sup>14</sup> Reid et al have postulated that the inclusion of S atom instead of N atom in amides can alter the molecular conformations as a result of S...O chalcogen bonding, which leads to a difference in their biological functions.<sup>15</sup> The strength and structural consequences of such contacts are still debated.<sup>16</sup> Considering the ubiquitous occurrence of S...O chalcogen bonds in a large number of drug molecules, the nature and robustness of this interaction motif needs to be quantitatively examined. In this paper, we have evaluated intramolecular S...O chalcogen bonding in acetazolamide, a diuretic drug (carbonic anhydrase I, II inhibitor) via experimental charge density analysis<sup>17</sup> and the quantum crystallographic technique of X-ray wavefunction refinement.<sup>18</sup> The conformational features of this molecule have been analysed by Nagao et al.<sup>19</sup> Their study suggested that intramolecular non-bonded S...O interaction in acetazolamide could regulate the molecular conformation even in the complex structures with enzymes. Acetazolamide molecule has been chosen for our study as it possesses two potential S...O chalcogen bonded ring motifs: (i) a four membered motif R(4), involving a sulfone oxygen atom, and (ii) a five membered motif R(5), involving a carbonyl oxygen atom (Fig 1). We have analysed these motifs in terms of the charge density topological

parameters, electron localization indicator<sup>20, 21</sup> (ELI-D) and Roby bond orders<sup>22</sup> derived from the ‘experimental wavefunction’ for acetazolamide. In addition, the strengths of intermolecular interactions have been examined for a comparison of various interaction motifs (particularly, the robustness of ‘sulfonamide dimer synthon’) as they have direct relevance in the area of crystal engineering of pharmaceutical co-crystals.

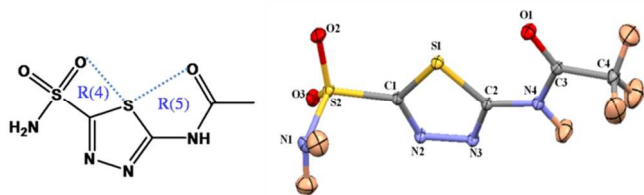


**Fig 1.** The molecular structure of acetazolamide and the ORTEP (with 50 % probability ellipsoids) obtained from the experimental charge density model.

### Experimental Crystallization

Acetazolamide (AZM) was obtained from Sigma-Aldrich and used without any further purification. The crystals were obtained from acetonitrile solvent by slow evaporation for 5 days.

### Data collecton and multipole refinement

High resolution data set for AZM was collected at 100K on an Oxford Xcalibur (Mova) diffractometer equipped with an Eos CCD detector using *MoK $\alpha$*  radiation ( $\lambda = 0.71073$  Å). The crystal to detector distance was fixed at 45 mm and the scan width ( $\Delta\omega$ ) was  $1^\circ$  per frame during the data collection. Cell refinement, data integration and reduction were carried out using the program CrysAlisPro and resulted in a redundancy ( $\sim 12$ ) and completeness of 100%. Numerical absorption correction was made after face indexing. Sorting, scaling, and merging of the data sets were carried out using the program SORTAV.<sup>23</sup> The multipole charge density modelling was performed using XD2015 (according to Hansen and Coppens multipole formalism)<sup>17, 24</sup> The function,  $\sum w [ |F_o|^2 - K |F_c|^2 ]^2$  was minimized for all reflections with  $I > 2\sigma(I)$ . Weights ( $w$ ) were taken as  $1/\sigma^2 (F_o^2)$  and the convergence criterion of the refinement was set to a maximal shift/esd  $< 10^{-9}$ . Su-Coppens-Macchi wave functions<sup>25</sup> were used for the core and valence scattering factors of all the atoms. The C—H and N—H bond lengths were constrained to neutron values<sup>26</sup> followed by the estimation of anisotropic thermal parameters using the SHADE2 analysis.<sup>27</sup> Separate  $\kappa$  and  $\kappa'$  were used to define different non-H atom type based chemical environments with a common  $\kappa$  for all H-atoms. For H atoms, only monopole, and bond directed dipole ( $d_z$ ) components were refined during the refinement. The scatter plots showing the variation of  $F_{obs}$  with  $F_{calc}$  is indicative of the good quality of the data set after scaling. The symmetric distribution of residual density in the fractal dimension plot shows the accuracy of the charge density model (Fig 2 and Fig 3). Crystallographic refinement details of both spherical and multipolar model are summarized in Table 1.

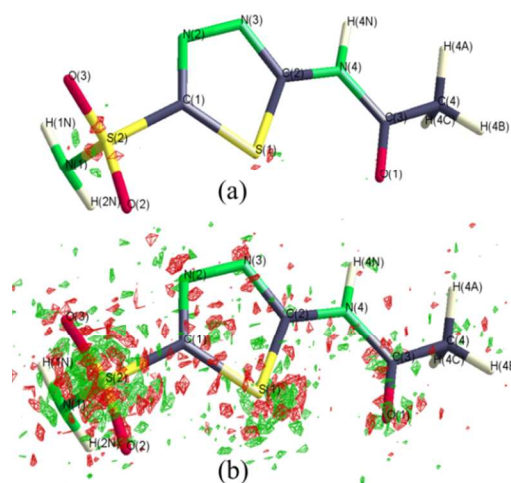


**Fig 2.** 3D residual density maps obtained from multipole model, plotted at contour levels of  $\pm 0.1 \text{ e}\text{\AA}^{-3}$  (a) and  $\pm 0.05 \text{ e}\text{\AA}^{-3}$  (b).

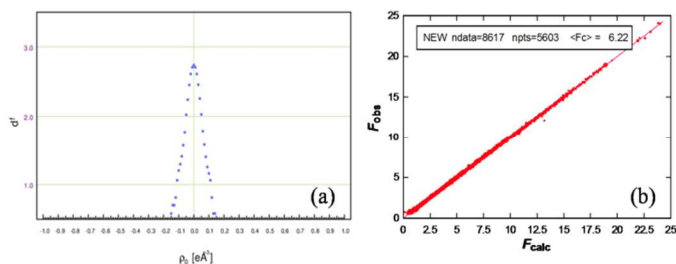


**Fig 3.** The fractal dimension plots of residual density from the experimental model and scatter plots depicting the variation of  $F_{obs}$  with  $F_{calc}$ .

**Table 1.** Crystallographic refinement details of spherical and multipolar models.

<b>Acetazolamide</b>		$(\sin\theta/\lambda)_{max} (\text{\AA}^{-1})$	1.0723
<i>Molecular formula</i>	$C_4H_6N_4O_3S_2$	<i>Reflns. collected</i>	109661
<i>Formula weight</i>	444.5	<i>Unique reflns.</i>	8617
<i>Crystal system</i>	Triclinic	<i>Completeness (%)</i>	99.5
<i>Space group</i>	<i>P</i> -1	<i>Redundancy</i>	12.7
<i>a</i> (Å)	5.2819(5)	<i>R<sub>int</sub></i>	0.034
<i>b</i> (Å)	8.9293(9)	<b>Spherical atom refinement</b>	
<i>c</i> (Å)	9.3525(9)	<i>R<sub>I</sub> (F)</i>	0.022
$\alpha$ (°)	104.658(9)	<i>wR<sub>2</sub> (F<sup>2</sup>)</i>	0.060
$\beta$ (°)	99.308(8)	<i>Goodness-of-fit</i>	1.048
$\gamma$ (°)	99.803(8)	$\Delta\rho_{min, max} (\text{e}\text{\AA}^{-3})$	-0.53, 0.67
<i>V</i> (Å <sup>3</sup> )	410.69(7)	<b>Multipole refinement</b>	
<i>Z</i>	2	<i>Reflns. used [I &gt; 2σ(I)]</i>	7915
$\rho_{calc} (\text{g}/\text{cm}^3)$	1.80	<i>Nref/Nv</i>	26.7
<i>F</i> (000)	227.9	<i>R<sub>I</sub> (F<sup>2</sup>)</i>	0.013
$\mu$ (mm <sup>-1</sup> )	0.628	<i>wR<sub>2</sub> (F<sup>2</sup>)</i>	0.034
<i>T</i> (K)	100(1)	<i>Goodness-of-fit</i>	0.923
$\lambda$ (Å)	0.71073	$\Delta\rho_{min, max} (\text{e}\text{\AA}^{-3})$	-0.15, 0.14

### X-ray wavefunction refinement (XWR)

The initial step of the XWR method involves Hirshfeld atom refinement (HAR).<sup>28</sup> In this procedure, a single-point molecular wavefunction calculation is performed on the starting geometry (in this study it is the geometry obtained from the multipole model). Further, Hirshfeld's stockholder scheme is used to partition the molecular electron density into atomic electron density fragments. The non-spherical atomic fragments thus obtained are used for scattering factors in a least squares refinement of positions and ADPs, in the subsequent steps. Energy calculation and least-squares refinement are repeated to convergence. Point charges and point dipoles on individual atomic sites are obtained following Hirshfeld's definition then placed around the molecule in HAR. In the next stage of XWR, an x-ray constrained wavefunction fitting is performed, in which the orbital coefficients are refined against the measured experimental diffraction data.

The refinement procedure involves the minimization of the term  $(E + \lambda\chi^2)$ , where  $E$  is the Hartree-Fock energy and  $\chi^2$  is the disagreement between the calculated and experimental structure factors.  $\chi^2$  is defined as follows:

$$\chi^2 = \frac{1}{N_r - N_p} \sum_i^{N_r} \frac{F(i)_{calc} - F(i)_{exp}}{\sigma^2(i)}$$

where,  $N_r$  and  $N_p$  are the numbers of reflections and parameters,  $\sigma^2(i)$  is the error in each structure factor, and  $F(i)_{calc}$  and  $F(i)_{exp}$  are the calculated and experimental structure factors, respectively.  $\lambda$  is a tunable parameter that determines the weight of the experimental data in the SCF calculation. XWR was carried out using the program TONTO<sup>29</sup> at HF/aug-ccPVTZ and blyp/def2TZVP levels. Both refinements yielded wavefunctions with satisfactory convergence (Table 2). The wavefunction from XWR at BLYP/def2TZVP level has been used to derive all the properties discussed in this study. This is a rare case where  $\chi^2=1$  agreement is achieved, which indicates the good quality of data treatment.

**Table 2.** Details of X-ray wavefunction refinement (XWR).

	HF/cc-pVTZ	BLYP/def2TZVP
R(F)	0.0130	0.0123
R <sub>w</sub> (F)	0.0166	0.0163
R(F <sup>2</sup> )	0.0306	0.0294
R <sub>w</sub> (F <sup>2</sup> )	0.0253	0.0249
S	1.001	1.001
$\chi^2$	1.003	1.002

### Results and discussions

Two main aspects of acetazolamide (in crystalline state) are discussed here; i) intermolecular interaction motifs, and ii) intramolecular S...O chalcogen bonding. Since the validity of intermolecular properties derived from XWR has not been established yet, we limit the discussion of intermolecular interactions to multipole derived charge densities and interaction energies. On the other hand, bond descriptors derived from XWR has been discussed mainly with regard to

the intramolecular bonds. Firstly, we describe the characteristics of intermolecular interaction motifs.

### Crystal structure description of acetazolamide

The crystal structure of acetazolamide was first reported by Mathew and Palenik<sup>30</sup> and later re-determined by Nagao et al.<sup>19</sup> It crystallizes in *P*-1 space group with  $Z=2$ .<sup>31</sup> The crystal structure shows N-H...N hydrogen bonded molecular dimeric assembly along with the N-H...O hydrogen bonds in sulfonamide dimer synthon and N-H...O<sub>(carbonyl)</sub> centrosymmetric dimer (Fig 4). The packing is further stabilized by C-H...O hydrogen bonds. It may be noted that acetazolamide is known for its reluctance to form co-crystals, and crystal engineers have rationalized this as a result of strong intermolecular interactions within its crystal structure.<sup>32</sup> In this context, we have analysed the intermolecular interaction motifs in quantitative terms in order to evaluate their strengths. For this, the crystal structure of AZM has been dissected into various molecular dimers as shown in Fig 5. The experimental charge density model provides a means to estimate the interaction energies corresponding to these motifs.

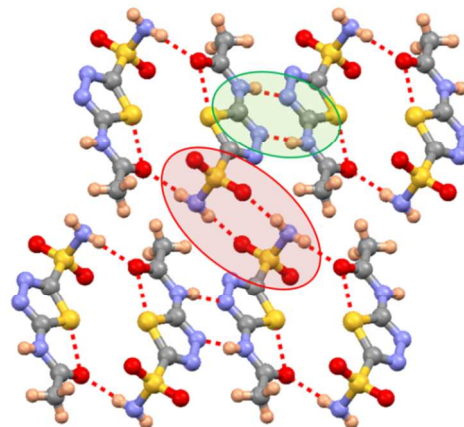


**Fig 4.** Crystal packing in acetazolamide showing the centrosymmetric N-H...N and N-H...O hydrogen bonded dimeric motifs (highlighted in green and red, respectively).

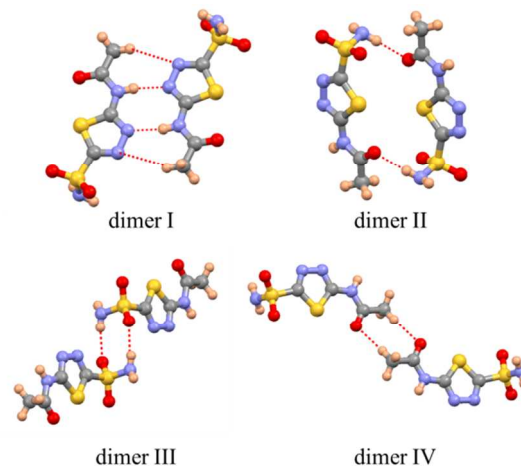


**Fig 5.** Various intermolecular dimer motifs that support crystal packing in acetazolamide.

### Estimation of intermolecular interaction energies from charge density topology

The electron density bond topological features at the bond critical points (BCPs) of inter and intramolecular interactions are given in Table 3. It is possible to use Abramov's expression<sup>33</sup> to obtain the kinetic energy density ( $G_{bcp}$ ) and the potential energy density  $V(r)$ , from the experimental charge density topological parameters such as electron density,  $\rho_{bcp}$  and its Laplacian,  $\nabla^2\rho_{bcp}$  (equations 1 and 2). In addition, the empirical relationship between kinetic energy density ( $G_{bcp}$ ), potential energy  $V(r)$  density and the interaction energy ( $E_{int}$ ) obtained by Espinosa et al<sup>34</sup> can be used to estimate the strengths of dimer motifs in AZM.

$$G_{bcp} = \frac{3}{10} (3\pi^2)^{\frac{2}{3}} \rho_{bcp}^{\frac{5}{3}} + \frac{\nabla^2\rho_{bcp}}{6} \quad (1)$$

$$V(r) = \frac{1}{4} \nabla^2\rho(r) - 2G(r) \quad (2)$$

$$E_{HB} = \frac{1}{2} V_{bcp} \quad (3)$$

It may be noted that the calculation of interaction energies

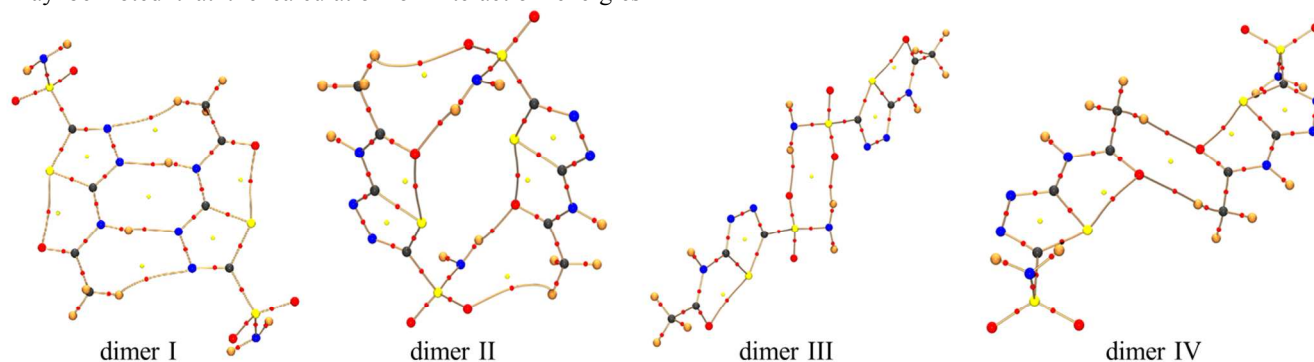


**Fig 6.** Molecular graphs showing intra and intermolecular bond paths and bond critical points (bcps, shown as small red spheres) for various molecular dimer motifs of AZM.

**Table 3.** Topological parameters and interaction energies (kJ/mol) derived for the intermolecular interactions in the crystal structure of acetazolamide calculated from EML method ( $E_{EML}$ ) and from the unperturbed wavefunction based method<sup>36</sup> in CrystalExplorer ( $E_{CE}$ ).

Interaction	$R_{ij}(\text{\AA})$	$d_1(\text{\AA})$	$d_2(\text{\AA})$	$\rho(\text{e}\text{\AA}^{-3})$	$\nabla^2\rho(\text{e}\text{\AA}^{-5})$	$\epsilon$	$E_{EML}(HB)$	$\Sigma E_{EML}(HB)$	$E_{CE}$
<b>Dimer I</b>									
<sup>c</sup> N4-H4N $\cdots$ N3	1.8326	0.5969	1.2357	0.213	3.419	0.09	-39.2	-84.6	-94.1
C4-H4A $\cdots$ N2	2.8015	1.6581	1.1434	0.03	0.48	0.51	-3.1		
<b>Dimer II</b>									
<sup>a</sup> N1-H2N $\cdots$ O1	1.8873	0.6601	1.2272	0.183	2.027	0.05	-27.6	-59.2	-90.0
C4-H4C $\cdots$ O2	2.9958	1.3460	1.6498	0.02	0.35	0.33	-2.0		
<b>Dimer III</b>									
<sup>b</sup> N1-H1N $\cdots$ O3	1.9713	0.6800	1.2913	0.099	2.093	0.01	-16.1	-32.2	-60.3
<b>Dimer IV</b>									
C4-H4B $\cdots$ O1	2.6368	1.0741	1.5627	0.03	0.51	0.08	-3.2	-6.4	-18.8
Symmetry operations: I) -x, -y, 1-z; II) 1-x, 1-y, 1-z; III) 1-x, -y, -z; IV) 1-x, 1-y, 2-z									

using the above expression (also known as the EML method) is purely based on the topological parameters at the BCPs, which reflects the local nature of electron density accumulation in the intermolecular region.

Fig 6 shows the bond paths representing various dimer motifs. Further, the hydrogen bond energies  $E_{HB}$  estimated from electron density,  $\rho_{bcp}$  and its Laplacian,  $\nabla^2\rho_{bcp}$  for different intermolecular bond paths in a dimer motif can be summed to obtain the net hydrogen bonding interaction energy for a dimer (given as  $\Sigma E_{EML}(HB)$  in Table 3). The hierarchy of interaction motifs thus obtained is: dimer I > dimer II > dimer III > dimer IV. The short N-H $\cdots$ N hydrogen bonds supported by C-H $\cdots$ N hydrogen bonds in dimer I results in very strong binding. Thus, dimer I represents a DDAA-AADD motif although one of the donors (C-H) is not a classical hydrogen bond donor (here A and D denote hydrogen bond acceptor and donor). In this contexts it is noteworthy that a similar AAAA-DDDD quadruple hydrogen-bond array<sup>35</sup> has been shown to be capable of directing supramolecular assembly even in solution and their thermodynamic stabilities (in terms of binding free energy,  $\Delta G$ ) have been found to be more than that of C-C covalent bonds.

Of the two hydrogen bond acceptor N atoms, the one which forms strong N–H $\cdots$ N hydrogen bond (N3) is different from the N atom which acts as an acceptor (N2) to a weak C–H $\cdots$ N hydrogen bond, in terms of electron density distribution (corresponding to the “lone pair” density). This feature is discussed in a latter section, in terms of electron localization indicator map (ELI) and deformation density. Similarly, dimer II formed by N–H $\cdots$ O<sub>(carbonyl)</sub> hydrogen bonds and dimer III formed by N–H $\cdots$ O<sub>(sulfonyl)</sub> hydrogen bonds also result in robust interaction motifs. The strength of the latter is noteworthy, as it is commonly referred to as “sulfonamide dimer synthon” in the context of crystal engineering (co-crystals and polymorphs).<sup>37</sup> Its interaction energy of -32.2 kJ/mol is comparable to that of carboxylic acid dimer or amide dimer as found from charge density topological parameters. Hence sulfonamide dimer synthon may be regarded as a strong motif capable of supporting crystal packing. The Laplacian maps showing the topological features of these interaction motifs are given in Fig7. Dimer IV is formed by C–H $\cdots$ O hydrogen bonds in a centrosymmetric fashion. The validity of such interaction motifs formed by C–H $\cdots$ O hydrogen bonds has been shown by us elsewhere.<sup>38</sup>

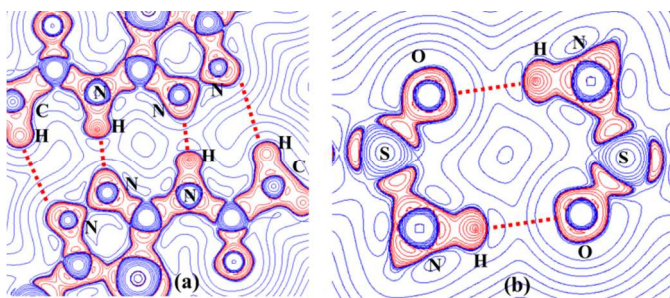


**Fig 7.** Laplacian map depicting (a) DDAA-AADD quadruple hydrogen-bond array in dimer I, and (b) sulfonamide dimer synthon region in dimer III (blue and red, represents positive and negative contours respectively, plotted in logarithmic scale).

Further, the values of binding energies estimated from charge densities have been compared with the interaction energies obtained from a molecular wavefunction based method in *CrystalExplorer*<sup>39</sup> (denoted as  $E_{CE}$  in Table 2). This method, introduced by Spackman, Jayatilaka and co-workers has been shown to yield surprisingly accurate values of interaction energies at cheap computational cost.<sup>36</sup> These energies are based on B3LYP/6-31G(d,p) molecular wavefunctions. It includes electrostatic, polarization, dispersion and exchange-repulsion terms, which are scaled to obtain accurate estimates of interaction energies benchmarked against B3LYP-D2/6-31G(d,p) counterpoise-corrected energies with a mean absolute deviation (MAD) of around 1 kJ mol<sup>-1</sup> (and a MAD of 2.5 kJ mol<sup>-1</sup> against CCSD(T)/CBS model energies). For the crystal structure of AZM, the interaction energies were calculated at the geometry obtained from the multipole model. It may be noted that the trends in the interaction hierarchy as obtained

from *CrystalExplorer*  $E_{CE}$  and  $\Sigma E_{EML}(\text{HB})$  values are the same, although their magnitudes are different. While  $E_{EML}(\text{HB})$  values provide an estimate of local characteristics of these hydrogen bond motifs,  $E_{CE}$  values represent the net molecule-molecule interactions, which have predominant electrostatic and dispersion terms. Thus AZM exhibits a robust interaction topology as revealed in its ‘energy framework’<sup>40</sup> (see ESI).

#### Intramolecular S $\cdots$ O chalcogen bonding

Further, we set out to analyse the charge density features of the intramolecular bonds and the S $\cdots$ O bond path in AZM. It is of fundamental importance to understand the geometrical criteria with respect to the relative orientation of donor and acceptor groups that lead to a realistic chalcogen bond. The S $\cdots$ O interaction geometry in the R(4) and R(5) motifs differ significantly from one another. The geometry of R(4) motif is such that it requires a ‘bent’ bond path from O atom to S atom for the chalcogen bond formation. The R(4) motif exhibits S $\cdots$ O interaction distance of 3.147 Å with a  $\angle\text{C-S}\cdots\text{O}$  angle of 139.26° (i.e.  $\angle\text{C2-S1}\cdots\text{O2}$ ). Similarly the R(5) motif shows a S $\cdots$ O interaction distance of 2.750 Å with a  $\angle\text{C-S}\cdots\text{O}$  angle of 157.39° (i.e.  $\angle\text{C1-S1}\cdots\text{O1}$ ). It may be noted that in both cases the interaction distances are within 3.32 Å – the van der Waals radii sum of S and O atoms. However, bond path analysis from the experimental charge density model shows that only the R(5) motif possesses realistic S $\cdots$ O interaction, and there exists no bond path that connects atoms S1 and O2 in the R(4) motif (see the molecular graphs in Fig 6). This illustrates the relevance of the angle  $\angle\text{X-O}\cdots\text{S}$  in chalcogen bond formation, where X is the atom connected to the chalcogen bond acceptor. In the R(4) motif,  $\angle\text{X-O}\cdots\text{S}$  (i.e.  $\angle\text{S2-O2}\cdots\text{S1}$ ) is 74.30° which is not favourable for an  $n(\text{O2})\rightarrow\sigma^*(\text{C2-S1})$  type interaction, as the lone pair density on O2 atom is not oriented adequately. The signatures of aspherical electron density distribution corresponding to the lone pairs and their orientations are seen in the static 3D deformation density map (Fig 8a).

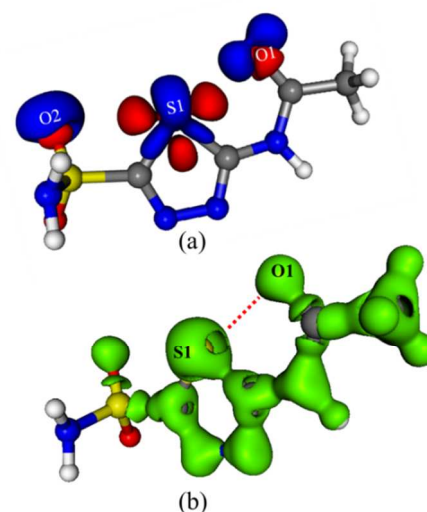


**Fig 8.** (a) Static 3D deformation density ( $\pm 0.005 \text{ e}\text{\AA}^{-3}$ ), and (b) Laplacian isosurface map ( $1.5 \text{ e}\text{\AA}^{-5}$ ).

Also, Lewis lone pair features on the chalcogen bond donor and acceptor atoms and their relative orientations can be seen from 2D Laplacian map (See ESI) as well as in electron localization indicator (ELI) map discussed in the next section. The 2D Laplacian map shows the valence shell charge concentration (VSCC) regions corresponding to the orientation of lone pair densities on S and O atoms. Hence, similar to the features reported in cases of sulfathiazole<sup>11</sup> and sulfamethizole<sup>5</sup>, the S $\cdots$ O chalcogen bond in AZM is also essentially an interaction that occurs between the charge concentrated (CC) region on O atom pointed towards the charge depleted (CD) region on S atom. While the CC-D orientation in R(5) motif in AZM favours S $\cdots$ O chalcogen bond, that is not the case with R(4) motif. A signature of this CC-CD nature can also be found in the 3D deformation density map (Fig 8a).

Murray and Politzer have classified halogen bonding and chalcogen bonding as  $\sigma$ -hole interactions,<sup>41</sup> as the structural origin of these interactions lies in the formation of electropositive regions around the electron acceptor halogen/chalcogen atom. This  $\sigma$ -hole feature can be found on the electrostatic potential (esp) surfaces of molecules. Hence, in order to examine the presence of  $\sigma$ -hole on S atoms in AZM, the esp was mapped on an isolated molecule extracted from the crystal lattice using the XD2015<sup>24</sup> and Molekel visualization software. The electropositive isosurface regions are indicated by blue colour whereas electronegative regions are displayed in red (Fig 9). The green area indicates neutral potential surfaces. The electrostatic potential around the S atom shows the  $\sigma$ -hole behaviour, i.e. a pair of electropositive regions on S atom along the C–S bond directions. The lone pair density around O and N atoms are seen as red regions on the esp surface and the hydrogen atoms are positively polarized as indicated by blue surfaces. Thus the CD-CC nature of the interaction is further substantiated by the features observed on esp map (Fig 9). Interestingly this  $\sigma$ -hole feature is found to be more pronounced on Laplacian surfaces (Fig 8b). Stalke et al have shown that a Laplacian zero-surface can be regarded as the ‘reactive surface’ of a molecule as it enables the visualization of electrophilic centres as holes on this surface.<sup>42</sup>

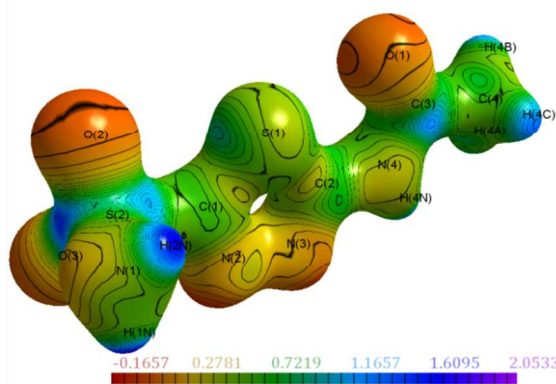


**Fig 9.** Electrostatic potential isosurface maps obtained from experimental charge density model of acetazolamide drawn at isosurface value of  $\pm 0.5 \text{ e}\text{\AA}^{-3}$ . Blue and red colours represent electropositive and electronegative regions, respectively.

We propose that the  $\sigma$ -holes on esp maps defined by Murray and Politzer (that lead to interactions such as halogen bonding and chalcogen bonding) can also be manifested as the ‘holes’ on the reactive surfaces represented by Laplacian isosurfaces. Recently we have shown similar ‘holes’ near a Se atom, on the Laplacian surface of the anti-oxidant ebselen, where it forms unusually short Se $\cdots$ O chalcogen bonds.<sup>4</sup> Hence in case of AZM, the  $\sigma$ -holes observed on Laplacian surface near S atom explains the origin of the S $\cdots$ O chalcogen bonding (Fig 8b). It may be noted that these features are observable at isosurfaces close to the zero-surface ( $\nabla^2\rho=0$ ). Interestingly similar ‘holes’ are observed near the C atoms C3 and C4. While C3 is a carbonyl carbon centre (the textbook-example for an electrophilic centre), the atom C4 exhibits features that might lead to a carbon bonding.<sup>9</sup> Thus, these ‘Laplacian holes’ provide significant chemical information, as they indicate centres where there is a probability of nucleophilic attack; that results in either a covalent bond or a non-bonded interaction.

The topological parameters evaluated at the bcp of the S $\cdots$ O interaction region are given in Table 4. The kinetic energy density,  $G(r_{\text{bcp}})$  and potential energy density,  $V(r_{\text{bcp}})$  calculated  $\rho_{\text{bcp}}$  and  $\nabla^2\rho_{\text{bcp}}$  of the S $\cdots$ O interaction bond path are  $41.66 \text{ kJ}\cdot\text{mol}^{-1}\text{bohr}^{-3}$  and  $-35.05 \text{ kJ}\cdot\text{mol}^{-1}\text{bohr}^{-3}$  respectively and their ratio  $|V|/G$  is 0.84. Fig10 shows the trend in variation of  $\rho_{\text{bcp}}$  and  $\nabla^2\rho_{\text{bcp}}$  with the S $\cdots$ O interaction distance from the reported experimental charge density studies<sup>5, 11, 13</sup> including this report.

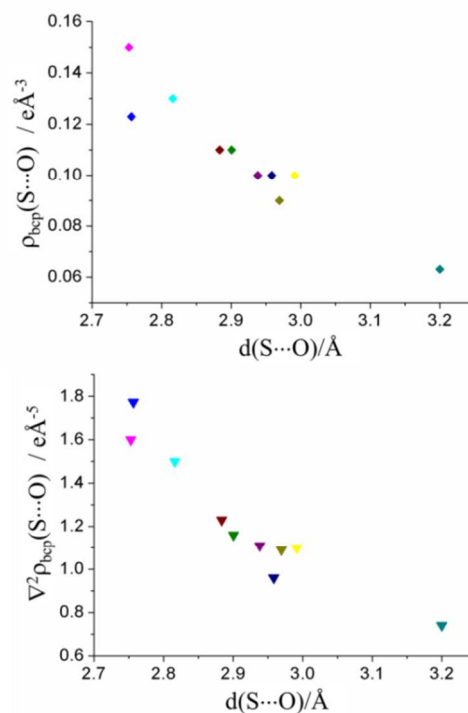


**Fig 10.** Variation of electron density,  $\rho_{\text{bcp}}$  and its Laplacian,  $\nabla^2\rho_{\text{bcp}}$  at the bcp with the S $\cdots$ O interaction distance (from experimental multipole models).

**Table 4.** Topological parameters of S...O chalcogen bond in AZM obtained from multipole model (MM), X-ray wavefunction refinement (XWR) and gas phase calculation at BLYP/def2TZVP level (G09).

	$R_{ij}(\text{\AA})$	$d_i(\text{\AA})$	$d_j(\text{\AA})$	$\rho(\text{e}\text{\AA}^{-3})$	$\nabla^2\rho(\text{e}\text{\AA}^{-5})$	$\varepsilon$
MM	2.7565	1.4421	1.3143	0.123	1.772	0.03
XWR	2.7519	1.4168	1.3351	0.140	0.422	0.23
G09	2.7523	1.4212	1.3311	0.142	0.426	0.23

#### Bond descriptors from the X-ray wavefunction

The S...O chalcogen bonding has been analyzed in terms of the bonding descriptors derived from the ‘experimental wavefunction’ (we use this term as the wavefunction is refined against experimental observations, although it might sound like an oxymoron!). X-ray constrained wavefunction refinement<sup>18, 43</sup> (XWR) protocol provides a means to refine the orbital coefficients of localized orbitals of an initial trial wavefunction. Using the advanced methodology of introducing point charges and dipoles corresponding to the neighboring molecules, it is possible to perturb the molecular wavefunction, loosely mimicking the crystal field effects. Hence it incorporates perturbation from crystalline electric field (as electrostatic moments of neighboring molecules) and that from the observed structure factors into a trial molecular wavefunction. Thus, by means of the minimization of the term  $(E + \lambda\chi^2)$ , XWR serves as a tool which combines variational and perturbation procedures to obtain the ‘experimental wavefunction’ of the molecule in crystal, from the X-ray diffraction data. The X-ray wavefunction thus obtained can be squared and integrated to obtain electron densities. The topological parameters of electron density obtained from X-ray wavefunction of AZM are comparable to those from the multipole charge density model (see graphs in Fig 11). It may be noted that while values of electron density  $\rho_{\text{bcp}}$  for intramolecular bonds from both the methods show reasonable agreement, the corresponding Laplacian values  $\nabla^2\rho_{\text{bcp}}$  do not match very well. Such a disagreement in  $\nabla^2\rho_{\text{bcp}}$  values has been obtained by Grabowsky, Jayatilaka and co-workers.<sup>44</sup> It was also found that the difference in values of  $\nabla^2\rho_{\text{bcp}}$  obtained from multipole and XWR methods are more pronounced for polar bonds. This observation is confirmed by the comparison of bond topological features in AZM. Table 4 shows the topological parameters for the intramolecular S...O bond path, obtained from XWR and that from the gas phase single point calculation using Gaussian09 and XWR geometry at blyp/def2-TZVP level (same level as XWR). This difference in values of  $\nabla^2\rho_{\text{bcp}}$  from MM and XWR is quite significant as it also points to a different nature of the S...O interaction. As a result the kinetic energy density,  $G(r_{\text{cp}})$  and potential energy density,  $V(r_{\text{cp}})$  corresponding to the S...O bcp are  $19.4 \text{ kJ}\cdot\text{mol}^{-1}\text{bohr}^{-3}$  and  $-27.4 \text{ kJ}\cdot\text{mol}^{-1}\text{bohr}^{-3}$  respectively. This leads  $|V(r_{\text{cp}})|/G(r_{\text{cp}})$  ratio of 1.41 which is significantly different from the  $|V(r_{\text{cp}})|/G(r_{\text{cp}})$  ratio of 0.84 obtained from multipole model. This is a matter of concern as the  $|V(r_{\text{cp}})|/G(r_{\text{cp}})$  ratio is widely considered to be a descriptor of the nature of interaction. A  $|V(r_{\text{cp}})|/G(r_{\text{cp}})$  ratio  $<1$  is often attributed to closed shell interaction, while a ratio  $>2$  is considered to be an open shell (covalent type) interactions. In

the case of S...O chalcogen bonding in AZM,  $|V(r_{\text{cp}})|/G(r_{\text{cp}})$  ratio of 1.41 indicates an intermediate nature (with a significant covalent/ open shell behaviour). Additionally the Laplacian isosurfaces for AZM exhibit  $\sigma$ -hole features as discussed in the previous section. Notably the differences in Laplacian values obtained from multipole and XWR methods are reflected on these surfaces. While the zero-surface does not exhibit  $\sigma$ -hole features, surfaces with  $\nabla^2\rho$  values close to zero (small negative values) show  $\sigma$ -holes (Fig 12). It should be noted that, on the Laplacian surfaces obtained from multipolar model, similar features are observed for small positive values  $\nabla^2\rho$ .

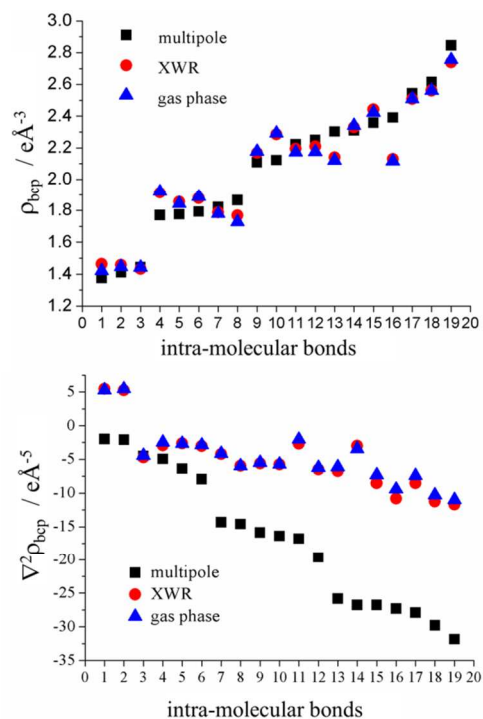


**Fig 11.** Comparison of electron density,  $\rho_{\text{bcp}}$  and its Laplacian,  $\nabla^2\rho_{\text{bcp}}$  obtained from multipole model, X-ray wavefunction, and a gas phase single point calculation.

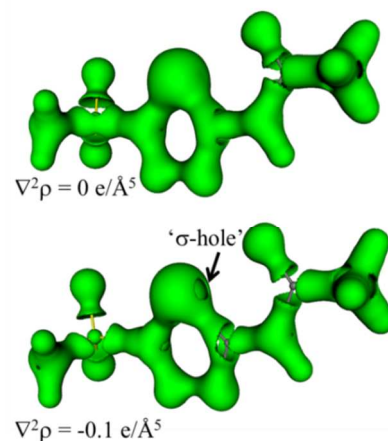


**Fig 12.** Laplacian isosurfaces obtained from X-ray wavefunction, plotted for  $\nabla^2\rho = 0 \text{ e}/\text{\AA}^5$  and  $\nabla^2\rho = -0.1 \text{ e}/\text{\AA}^5$ .

### Electron Localizability Indicator (ELI)

Further, the ELI-D variant<sup>21</sup> of the ELI has been calculated for AZM from the X-ray wavefunction. Essentially this descriptor indicates the probability of same spin electron pairing in space. ELI-D value at any point in space is equal to a product of a particular spin electron density (say  $\alpha$ ) and a volume factor related to same spin pairing. i.e.

$$\text{ELI}_D = \rho_\alpha(\vec{r}) \cdot \tilde{V}_{D\alpha\alpha}(\vec{r})$$

where the volume factor  $\tilde{V}_{D\alpha\alpha}(\vec{r})$  at each point is proportional to the volume required to enclose an arbitrary fraction of the same spin electron pair.<sup>45</sup> It is to be noted that the different points on an isoelectron density surface of a molecule would have different values of  $\text{ELI}_D$  as the same spin-pairing propensity around each such point may be different. The first term in the expression for  $\text{ELI}_D$ , the density of a particular spin electron,  $\rho_\alpha$  is straight forward to imagine. In order to conceptualize  $\tilde{V}_{D\alpha\alpha}(\vec{r})$ , one may imagine a “bubble” around each such point where the volume of the bubble is determined such that it encloses a fixed fraction of same spin pair. Hence, points where larger volume elements are required to capture the same-spin pair-fraction will have larger values of  $\text{ELI}_D$ . Hence a large value of  $\text{ELI}_D$  corresponds to a region of lower pair density of same-spin electrons. It may be noted that the Lewis picture of electron pairs often described by chemists refers to opposite-spin electron pairs. In closed-shell spin-restricted singlet cases,  $\rho_\alpha$  and  $\rho_\beta$  are the same. Hence, a high  $\text{ELI}_D$  can correspond to a high localization of both  $\alpha$  and  $\beta$  spin electrons.

Notably the  $\text{ELI}_D$  isosurface (surface with an arbitrary value of  $\text{ELI}_D$ ) plotted for AZM exhibits the electron pair features corresponding to intra molecular S $\cdots$ O chalcogen bond and intermolecular hydrogen bonds. Figure 13 shows the  $\text{ELI}_D$  map for AZM (plotted for  $\text{ELI}_D=1.45$ ) in comparison with the static 3D deformation density map. (it is remarkable that static deformation density map shows certain similarity with  $\text{ELI}_D$  map in its shape). Thus the classical “lone pair” features can be visualized. The ELI features on S and O atoms involved in the

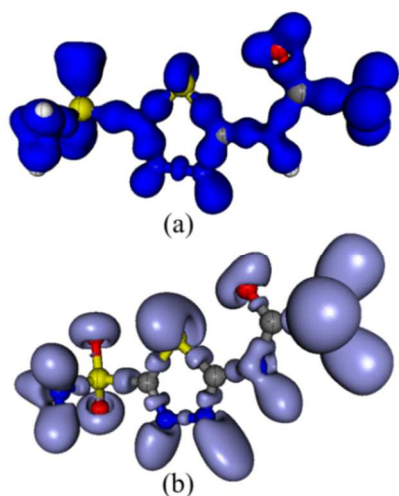


**Fig 13** Static 3D deformation density map ( $0.03 \text{ e}/\text{\AA}^3$ ) obtained from X-ray wavefunction, and  $\text{ELI}_D$  surface for  $\text{ELI}_D=1.45$ .

S $\cdots$ O chalcogen bond are particularly interesting, as the lone pair density on O atom is oriented to a region of less electron pairing on S atom. This is consistent with the observations from 3D Laplacian maps. More interestingly, the ELI features around N2 and N3 atoms in the five membered ring of AZM differ significantly, although their bonding types are very similar (visualized as “sp<sup>2</sup> hybridized” N atoms by chemists). While N2 exhibits a smaller lobe of ELI surface, that around N3 is found to be a much larger elongated lobe. This may be understood as a consequence of difference in intermolecular hydrogen bonding exhibited by these two N atoms. While N3 forms a very short N–H $\cdots$ N hydrogen bond, N2 forms only a weak C–H $\cdots$ N hydrogen bond (Table 2). Hence, the enhanced electron delocalization due to stronger hydrogen bond formed by N3 manifests as a larger lobe in  $\text{ELI}_D$  map.

### Roby bond indices

Roby bond indices have been estimated for AZM using the X-ray wave function. A covalent bond is generally understood as a pair of electrons shared between two bonded atoms. For diatomic molecules, bond order is estimated as half the difference between the number of electrons in the bonding and anti-bonding orbitals. For larger molecules, more complex bond indicators are required to describe bond orders. The Roby bond index<sup>22</sup> introduced by Jayatilaka et al is a descriptor developed based on Roby’s projection operator theory. Using Roby operator  $R$  and an ionic operator  $I$  the degree of covalent and ionic nature associated with chemical bonds can be calculated. While the sharing of electronic population between a pair of atoms implies covalency, the transfer of population between them indicates ionicity. The utility of this bond descriptor has been demonstrated by Grabowsky et al, in the context of ionic type S–O bond in  $\text{SO}_2$ .<sup>43</sup> The Roby bond orders obtained for AZM has been shown in Fig 14. It is found that the bond orders for the sulfonyl S–O bonds in AZM are similar to those reported for the phenyl sulfone functional group reported by Grabowsky et al.<sup>43</sup> That the percentage covalencies of the S–O bonds obtained for AZM (from Roby covalency operator) are nearly 90% underpins the partial ionic nature of these bonds.

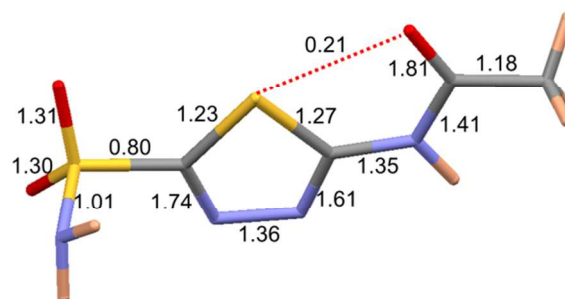


**Fig 14** Roby bond orders for S $\cdots$ O interaction and various covalent bonds in AZM.

It is interesting to note the partial double bond character for most of the bonds in AZM, which is in agreement with the resonance picture of the molecule. The bond order for intramolecular S $\cdots$ O chalcogen bond was found to be 0.21. This is remarkable for a non-bonding interaction, especially when the N–H and C–H covalent bonds exhibit bond orders of nearly one (details of Roby bond orders for all bonds are given in ESI). Further, the eigen values of Roby operator indicates a covalent nature for the S $\cdots$ O interaction. This is not fully consistent with the inference from the  $V(r_{cp})/G(r_{cp})$  ratio for the S $\cdots$ O BCP obtained from the XWR densities, the reason for which is not understood.

### Conclusions

In summary, we have quantitatively evaluated the strengths of inter and intramolecular interactions in acetazolamide using the descriptors from multipole model and X-ray wavefunction. The observation of strong interaction motifs in its crystal structure rationalizes the known reluctance of AZM towards co-crystal formation. Even though the values of intermolecular interaction energies estimated via EML method and that from *CrystalExplorer* differ, the ranking of dimeric motifs remains the same. A comparison of topological properties of various covalent bonds ( $\nabla^2\rho_{bcp}$ ) obtained from multipole model and XWR shows that the values of electron density at the BCPs match, while those of Laplacian differ significantly. The intramolecular S $\cdots$ O chalcogen bond has been characterized in terms of topological parameters of charge density. The ‘ $\sigma$ -hole’ features on S atom that lead to S $\cdots$ O chalcogen bond have been visualized on ESP map and Laplacian isosurfaces. ELI-D map shows the relative orientations of lone pair densities around S and O atoms that lead to CC-CD type interaction. This highlights the effect of ‘orbital geometry’ (as it is present in the classical Lewis picture) on the donor and acceptor atoms in the formation of chalcogen bonding. Interestingly, the ELI-D map shows similarity with rather simple 3D deformation density map. Further, Roby bond orders, shared population parameter, and  $|V(r_{cp})|/G(r_{cp})$  ratio obtained from X-ray wavefunction provides insights into the strength of S $\cdots$ O chalcogen bond and its covalent (electron sharing) nature.

We dedicate this paper to Mr. K. R. Sivanandan, an excellent teacher of physics and chemistry at GVHSS Mogral, Kerala, on the occasion of his retirement. SPT thanks Prof Mark Spackman for the access to *CrystalExplorer* and M. S. Pavan for help. TNG thanks DST for the J. C. Bose fellowship.

### Notes and references

<sup>a</sup>School of Chemistry and Biochemistry, The University of Western Australia, Crawley, WA, Australia. E-mail: sajesh.thomas@uwa.edu.au

<sup>b</sup>Solid state and Structural Chemistry Unit, Indian Institute of Science, Bangalore, India, 560012. E-mail: sstng@sscu.iisc.ernet.in

1. C. R. Jones, P. K. Baruah, A. L. Thompson, S. Scheiner and M. D. Smith, *J Am Chem Soc*, 2012, **134**, 12064-12071; S. Aravinda, N. Shamala, A. Pramanik, C. Das and P.

- Balar, *Biochem. and Biophys. Res. Commun.*, 2000, **273**, 933-936; S. P. Thomas, K. Nagarajan and T. N. G. Row, *Chem Commun*, 2012, **48**, 10559-10561; S. P. Thomas, K. Shashiprabha, K. R. Vinutha, S. P. Nayak, K. Nagarajan and T. N. G. Row, *Cryst Growth Des*, 2014, **14**, 3758-3766.
2. P. Metrangolo, F. Meyer, T. Pilati, G. Resnati and G. Terraneo, *Angew. Chem. Int. Ed.*, 2008, **47**, 6114-6127.
3. P. Metrangolo, H. Neukirch, T. Pilati and G. Resnati, *Acc Chem Res*, 2005, **38**, 386-395.
4. S. P. Thomas, K. Satheeshkumar, G. Mugesh and T. N. Guru Row, *Chem. Eur. J.*, 2015, **21**, 6793-6800.
5. S. P. Thomas, S. P. K. P. Veccham, L. J. Farrugia and T. N. Guru Row, *Cryst Growth Des*, 2015, **15**, 2110-2118.
6. M. Bai, S. P. Thomas, R. Kottokkaran, S. K. Nayak, P. C. Ramamurthy and T. N. G. Row, *Cryst Growth Des*, 2014, **14**, 459-466; W. Wang, B. Ji and Y. Zhang, *J. Phys. Chem. A*, 2009, **113**, 8132-8135; M. E. Brezgunova, J. Lieffrig, E. Aubert, S. Dahaoui, P. Fertey, S. Lebegue, J. G. Angyan, M. Fourmigue and E. Espinosa, *Cryst Growth Des*, 2013, **13**, 3283-3289; S. P. Thomas, R. Sathishkumar and T. N. Guru Row, *Chem. Commun.*, 2015, 10.1039/c5cc03322e.
7. S. Sarkar, M. S. Pavan and T. N. Guru Row, *Phys Chem Chem Phys*, 2015, **17**, 2330-2334; S. Scheiner, *Acc Chem Res*, 2013, **46**, 280-288.
8. D. Mani and E. Arunan, *Phys Chem Chem Phys*, 2013, **15**, 14377-14383.
9. S. P. Thomas, M. S. Pavan and T. N. Guru Row, *Chem Commun (Camb)*, 2014, **50**, 49-51.
10. P. Metrangolo and G. Resnati, *Nature chemistry*, 2012, **4**, 437-438; D. Manna and G. Mugesh, *J Am Chem Soc*, 2012, **134**, 4269-4279.
11. I. Sovago, M. J. Gutmann, J. G. Hill, H. M. Senn, L. H. Thomas, C. C. Wilson and L. J. Farrugia, *Cryst Growth Des*, 2014, **14**, 1227-1239.
12. R. Destro, R. Soave, M. Barzaghi and L. Lo Presti, *Chem-Eur J*, 2005, **11**, 4621-4634.
13. R. Soave, M. Barzaghi and R. Destro, *Chem-Eur J*, 2007, **13**, 6942-6956.
14. V. d. P. N. Nziko and S. Scheiner, *J. Organic Chem.*, 2015, **80**, 2356-2363.
15. R. C. Reid, M. K. Yau, R. Singh, J. X. Lim and D. P. Fairlie, *J Am Chem Soc*, 2014, **136**, 11914-11917.
16. N. E. Jackson, B. M. Savoie, K. L. Kohlstedt, M. O. de la Cruz, G. C. Schatz, L. X. Chen and M. A. Ratner, *J Am Chem Soc*, 2013, **135**, 10475-10483.
17. T. S. Koritsanszky and P. Coppens, *Chem. Rev.*, 2001, **101**, 1583-1627.
18. D. Jayatilaka, *Physical Review Letters*, 1998, **80**, 798-801; D. Jayatilaka and D. J. Grimwood, *Acta Cryst. A*, 2001, **57**, 76-86.
19. Y. Nagao, T. Honjo, H. Iimori, S. Goto, S. Sano, M. Shiro, K. Yamaguchi and Y. Sei, *Tetrahedron Lett*, 2004, **45**, 8757-8761.
20. M. Kohout, *Faraday Discussions*, 2007, **135**, 43-54; M. Kohout, *Int J Quantum Chem*, 2004, **97**, 651-658.

21. F. R. Wagner, M. Kohout and Y. Grin, *The Journal of Physical Chemistry A*, 2008, **112**, 9814-9828.
22. M. Gould, C. Taylor, S. Wolff, G. Chandler and D. Jayatilaka, *Theor Chem Account*, 2008, **119**, 275-290.
23. R. H. Blessing, *J Appl Crystallogr*, 1997, **30**, 421-426.
24. A. Volkov, P. Macchi, L. J. Farrugia, C. Gatti, P. Mallinson, T. Richter and T. Koritsanszky, *XD-2015 - A computer program for multipole refinement, topological analysis of charge densities and evaluation of intermolecular energies from experimental or theoretical structure factors*, 2015.
25. P. Macchi and P. Coppens, *Acta Cryst. A*, 2001, **57**, 656-662; Z. W. Su and P. Coppens, *Acta Cryst. A*, 1998, **54**, 357-357.
26. F. H. Allen and I. J. Bruno, *Acta Cryst. B*, 2010, **66**, 380-386.
27. A. O. Madsen, *J Appl Crystallogr*, 2006, **39**, 757-758; P. Munshi, A. O. Madsen, M. A. Spackman, S. Larsen and R. Destro, *Acta Cryst. A*, 2008, **64**, 465-475.
28. S. C. Capelli, H.-B. Burgi, B. Dittrich, S. Grabowsky and D. Jayatilaka, *IUCrJ*, 2014, **1**, 361-379; M. Woinska, D. Jayatilaka, M. A. Spackman, A. J. Edwards, P. M. Dominiak, K. Wozniak, E. Nishibori, K. Sugimoto and S. Grabowsky, *Acta Cryst. A*, 2014, **70**, 483-498.
29. D. Jayatilaka and D. Grimwood, in *Computational Science — ICCS 2003*, eds. P. A. Sloot, D. Abramson, A. Bogdanov, Y. Gorbachev, J. Dongarra and A. Zomaya, Springer Berlin Heidelberg, 2003, vol. 2660, pp. 142-151.
30. M. Mathew and G. J. Palenik, *Journal of the Chemical Society, Perkin Transactions 2*, 1974, 532-536.
31. It may be noted that Nagao et al reported a 93 K data (ref 19), and Mathew et al reported a room temperature data for the same (ref 30). Our data set was collected at 100 K and hence the small differences in cell parameters from those in ref 19. A monoclinic polymorph of acetazolamide is also known: U. J. Griesser, A. Burger, K. Mereiter, *J. Pharm. Sci.* 1997, **86** (3), 352.
32. S. Varughese, S. Sinha and G. Desiraju, *Sci. China Chem.*, 2011, **54**, 1909-1919; J. I. Arenas-García, D. Herrera-Ruiz, K. Mondragón-Vásquez, H. Morales-Rojas and H. Höpfl, *Cryst Growth Des*, 2010, **10**, 3732-3742.
33. Y. A. Abramov, *Acta Cryst. A*, 1997, **53**, 264-272.
34. E. Espinosa, I. Alkorta, I. Rozas, J. Elguero and E. Molins, *Chem Phys Lett*, 2001, **336**, 457-461; E. Espinosa and E. Molins, *J Chem Phys*, 2000, **113**, 5686-5694.
35. B. A. Blight, C. A. Hunter, D. A. Leigh, H. McNab and P. I. T. Thomson, *Nature chemistry*, 2011, **3**, 244-248.
36. M. J. Turner, S. Grabowsky, D. Jayatilaka and M. A. Spackman, *J. Phys. Chem. Lett.*, 2014, **5**, 4249-4255.
37. P. Sanphui, B. Sarma and A. Nangia, *Cryst Growth Des*, 2010, **10**, 4550-4564; G. Bolla, S. Mittapalli and A. Nangia, *IUCrJ*, 2015, **2**.
38. S. P. Thomas, M. S. Pavan and T. N. G. Row, *Cryst Growth Des*, 2012, **12**, 6083-6091.
39. S. K. Wolff, D. J. Grimwood, J. J. McKinnon, M. J. Turner, D. Jayatilaka and M. A. Spackman, *CrystalExplorer (Version 4-unreleased)*, 2015.
40. M. J. Turner, S. P. Thomas, M. W. Shi, D. Jayatilaka and M. A. Spackman, *Chem Commun*, 2015, **51**, 3735-3738.
41. J. S. Murray, P. Lane and P. Politzer, *Int J Quantum Chem*, 2008, **108**, 2770-2781; P. Politzer, J. S. Murray and T. Clark, *Phys Chem Chem Phys*, 2013, **15**, 11178-11189; P. Politzer, J. S. Murray and T. Clark, *Phys Chem Chem Phys*, 2010, **12**, 7748-7757.
42. D. Leusser, J. Henn, N. Kocher, B. Engels and D. Stalke, *J Am Chem Soc*, 2004, **126**, 1781-1793; D. Stalke, *Chem-Eur J*, 2011, **17**, 9264-9278.
43. S. Grabowsky, P. Luger, J. Buschmann, T. Schneider, T. Schirmeister, A. N. Sobolev and D. Jayatilaka, *Angew. Chem.*, 2012, **51**, 6776-6779.
44. M. Woinska, P. Dominiak, K. Wozniak, D. Jayatilaka, S. J. Grabowsky (private communication).
45. S. Grabowsky, M. Weber, D. Jayatilaka, Y.-S. Chen, M. T. Grabowski, R. Brehme, M. Hesse, T. Schirmeister and P. Luger, *J. Phys. Chem. A*, 2011, **115**, 12715-12732.